Inorganic Chemistry

pubs.acs.org/IC Article

A Low-Temperature Structural Transition in Canfieldite, Ag_8SnS_6, Single Crystals

Tyler J. Slade,* Volodymyr Gvozdetskyi, John M. Wilde, Andreas Kreyssig, Elena Gati, Lin-Lin Wang, Yaroslav Mudryk, Raquel A. Ribeiro, Vitalij K. Pecharsky, Julia V. Zaikina, Sergey L. Bud'ko, and Paul C. Canfield*

Cite This: *Inorg. Chem.* 2021, 60, 19345−19355 Read Online

ACCESS | Metrics & More | Article Recommendations | Supporting Information

ABSTRACT: Canfieldite, Ag_8SnS_6, is a semiconducting mineral notable for its high ionic conductivity, photosensitivity, and low thermal conductivity. We report the solution growth of large single crystals of Ag_8SnS_6 of mass up to 1 g from a ternary Ag−Sn−S melt. On cooling from high temperature, Ag_8SnS_6 undergoes a known cubic ($F\bar{4}3m$) to orthorhombic ($Pna2_1$) phase transition at ≈460 K. By studying the magnetization and thermal expansion between 5−300 K, we discover a second structural transition at ≈120 K. Single crystal X-ray diffraction reveals the low-temperature phase adopts a different orthorhombic structure with space group $Pmn2_1$ (a = 7.662 9(5) Å, b = 7.539 6(5) Å, c = 10.630 0(5) Å, Z = 2 at 90 K) that is isostructural to the room-temperature forms of the related Se-based compounds Ag_8SnSe_6 and Ag_8GeSe_6. The 120 K transition is first-order and has a large thermal hysteresis. On the basis of the magnetization and thermal expansion data, the room-temperature polymorph can be kinetically arrested into a metastable state by rapidly cooling to temperatures below 40 K. We last compare the room- and low-temperature forms of Ag_8SnS_6 with its argyrodite analogues, Ag_8TQ_6 (T = Si, Ge, Sn; Q = S, Se), and identify a trend relating the preferred structures to the unit cell volume, suggesting smaller phase volume favors the $Pna2_1$ arrangement. We support this picture by showing that the transition to the $Pmn2_1$ phase is avoided in Ge alloyed $Ag_8Sn_{1-x}Ge_xS_6$ samples as well as in pure Ag_8GeS_6.

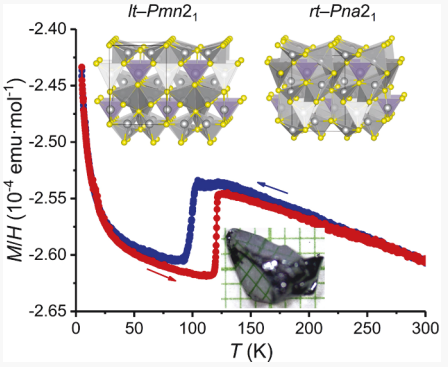

1. INTRODUCTION

Multinary silver chalcogenides exhibit rich structural chemistry and electronic properties that generate both fundamental and technological interest. A hallmark of these compounds is weak bonding between silver and chalcogenide atoms, often resulting in diverse crystal structures, substantial anharmonic atomic displacements, site occupancy disorder, and/or metal atoms in unique, distorted coordination environments.[1−4] Consequentially, many silver chalcogenides have high ionic conductivity and a tendency to undergo phase transitions upon heating or cooling.[5−8] The soft bonding and structural complexity can give rise to low phonon velocities and intrinsically glasslike thermal conductivity. As such, many silver chalcogenides are attractive thermoelectric materials.[9−15] Compared to oxides, the bonds in metal chalcogenides are generally more covalent, which affords smaller band gaps and higher charge carrier mobility,[16] making some chalcogenides promising for solar energy conversion.[17]

The past decades witnessed impressive advancement in the synthesis of chalcogenide materials. Whereas the high vapor pressures and low boiling points of the chalcogens, particularly sulfur, are challenges for the growth of large single crystals of chalcogen-rich compounds, solution or flux techniques have proven invaluable for their ability to permit chemical reactions and crystallization at moderate temperatures compared to traditional solid state methods.[18−20] In this regard, polychalcogenide salts are powerful solvents for the synthesis of alkali metal and main group chalcogenide compounds.[20,21] Low-melting binary metal−sulfur compositions or eutectics can also be effective starting points for solution growth of sulfur-rich materials.[18]

Canfieldite,[22] Ag_8SnS_6, is a mineral belonging to the family of closely related argyrodite compounds.[2] Like all argyrodites, Ag_8SnS_6 adopts a high-temperature (ht) cubic crystal structure with the $F\bar{4}3m$ space group that features a highly disordered Ag sublattice in which the Ag ions are distributed over three partially occupied crystallographic sites. Previous work indicates that at 460 K, Ag_8SnS_6 undergoes a transition from the ht cubic phase to the room-temperature (rt) orthorhombic structure with space group $Pna2_1$.[2,23,24] Upon heating, the structural transition can be visualized as the Ag sublattice

Received: October 12, 2021
Published: December 10, 2021

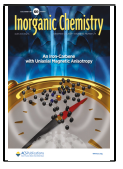

https://doi.org/10.1021/acs.inorgchem.1c03158
Inorg. Chem. 2021, 60, 19345−19355

"melting" into the highly disordered state while the Sn and S framework remains essentially rigid, or intact. As a consequence, the ht phase has high ionic conductivity supported by mobile Ag^+ ions. The heavy disorder in the "liquid like" Ag sublattice facilitates exceptionally strong phonon scattering, and the lattice thermal conductivity of ht-Ag_8SnS_6 approaches the theoretical amorphous minimum.[24] Accordingly, recent work demonstrates that ht-Ag_8SnS_6 is a promising thermoelectric material with a figure of merit zT of 0.8 near 773 K when alloyed with Se.[24,25] Most work on the rt, orthorhombic, variant is concerned with nanocrystals,[26−28] which have been prepared and studied as counter electrodes in solar cells and for photocatalytic water splitting and dye degradation.[29−31] Notably, the rt phase has a band gap of approximately 1.4 eV and high absorption coefficient of 10^4 cm^{-1} in the visible range,[32] making rt Ag_8SnS_6 a potential light absorber for photovoltaic applications.[33,34]

Whereas both the ambient and ht forms of Ag_8SnS_6 exhibit interesting properties and structural chemistry, the evolution of the crystal structure and physical properties below room temperature are yet to be reported. Here, we demonstrate solution growth of large (≈ 1 g) single crystals of Ag_8SnS_6 out of a Sn−S rich ternary melt, and by use of temperature-dependent magnetization, thermal expansion, and X-ray diffraction measurements, we identify a previously unreported first-order structural phase transition at 120 K. We find that below 120 K, Ag_8SnS_6 can adopt a different low-temperature (lt) orthorhombic structure with the $Pmn2_1$ space group that is isostructural to the rt forms of the related Se-based compounds Ag_8SnSe_6 and Ag_8GeSe_6. The rt to lt structural phase transition has large thermal hysteresis, and the magnetization and thermal expansion results indicate that the rt phase can be kinetically arrested by rapid cooling into a metastable state below 40 K. By comparing the room- and low-temperature Ag_8SnS_6 polymorphs with the preferred structures of the argyrodite analogues Ag_8TQ_6 (T = Si, Ge, Sn; Q = S, Se), we suggest that lower volume unit cells (normalized per formula unit) favor the rt $Pna2_1$ form. We support this picture by applying chemical pressure, that is, reducing the unit cell volume, to Ag_8SnS_6 by partially replacing Sn with Ge, and find the rt $Pna2_1$ phase is preserved down to 5 K in $Ag_8Sn_{1-x}Ge_xS_6$ and pure Ag_8GeS_6. Lastly, we use density functional theory calculations to discuss the role of Ag−S bonding in dictating the energetically preferred structure.

2. EXPERIMENTAL DETAILS

Crystal Growth. Both of the Ag−S and Sn−S binary phase diagrams have accessible liquid regions for compositions near Ag_2S and compositions between SnS_2 and SnS with eutectic temperatures as low as 740 °C.[35−37] Perhaps more importantly, studies of parts of the ternary Ag−Sn−S phase diagram indicate the existence of an exposed liquidus surface for the primary formation of Ag_8SnS_6.[38] On the basis of the existing phase diagram data, as well as our experience with S-based growths, we used Ag_2S (Alfa-Aesar, 99.5%), S (Alfa-Aesar 99.99%), and Sn (Alfa-Aesar, 99.99%) in a molar ratio 35:38:27, respectively, giving a stoichiometry of $Ag_{41}Sn_{16}S_{43}$ as the initial composition of our melt. The reactions used approximately 3 g total of starting reagents.

To test our ability to safely grow Ag_8SnS_6 out of the ternary melt in a well controlled manner, we first placed the Ag_2S−S−Sn mixture into a 2 ml fritted alumina crucible set,[39] sealed the crucible set into an amorphous silica ampule under a 1/4 atm of high purity Ar, and gradually heated to 800 °C over 10 h. After holding at 800 °C for 10 h, the ampule was removed from the furnace, inverted into a centrifuge, and decanted.[39,40] All of the materials passed through the frit with (i) no apparent attack on the alumina crucible, (ii) no evaporative loss of material from the crucible, (iii) no evidence for overpressure in the growth ampule. On the basis of these results, we performed a second growth, again heating to 800 °C, dwelling for 10 h, and then cooling over 200 h to 625 °C. After decanting the excess liquid, large, mirror-faceted, single crystals of Ag_8SnS_6 weighing up to 1 g with dimensions as large as 5−10 mm were recovered (see the inset of Figure 1). Ge alloyed samples were prepared in the same manner, substituting elemental Ge (Alfa-Aesar, 99.99%) for Sn using initial compositions of $Ag_{41}(Sn_{1-x}Ge_x)_{16}S_{43}$ to produce single crystals of $Ag_8Sn_{1-x}Ge_xS_6$ (x = 0.1, 0.25, 1).

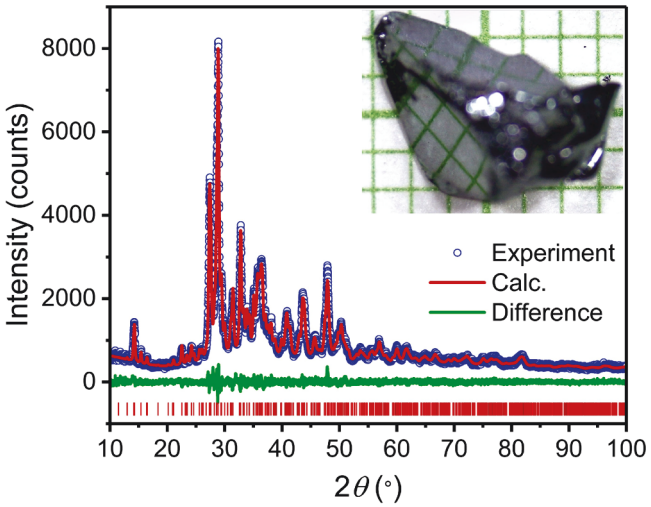

Figure 1. Powder X-ray diffraction pattern obtained on a powdered crystal of Ag_8SnS_6. The solid lines are the fitted results of a Rietveld refinement and are in good agreement with the rt $Pna2_1$ structure of Ag_8SnS_6 with refinement statistics R_{wp} = 4.95 and GOF = 1.39. The inset is a picture of a flux grown crystal on a mm grid; the grid is reflected in two of the facets.

Powder X-ray Diffraction. To confirm the structure and phase purity of the flux grown crystals, samples were analyzed with powder X-ray diffraction (PXRD). Pieces of the crystals were ground by hand in a mortar and pestle to a fine powder, sifted through a 35 μm mesh sieve, and diffraction patterns were collected at room temperature on a Rigaku Miniflex-II instrument operating with Cu Kα radiation (λ = 1.540 6 Å) at 30 kV and 15 mA. The crystal structure was refined using the Rietveld method with GSAS-II software.[41]

Magnetization. Temperature-dependent magnetization measurements were performed in Quantum Design Magnetic Property Measurement System (MPMS-classic and MPMS-3) SQUID magnetometers operating in the DC measurement mode and in a field of 10 kOe. To avoid potential oxygen adsorption on the surface of the samples, several randomly oriented crystals (total mass ∼80 mg) of Ag_8SnS_6 were sealed in a partial argon atmosphere between two fused silica rods of similar length in a fused silica tube. The length of the rods and the tube were such that the only additional contribution to the magnetic signal from the assembly comes from the gap between the rods in which the samples are contained. This contribution was subtracted using the size of the gap and previous calibration. The powder samples were measured in a gel capsule which was mounted in a straw. To allow for evacuation, pinholes were poked in the straw and in the top of the capsule. For the powder samples, a separate background from an empty capsule was measured and subtracted. The measurements were conducted between 5−300 K with a heating/cooling rate of 0.5 K·min^{-1} between each temperature step. To study hysteresis and lt metastability, we also quenched (cooled as rapidly as possible, at ≈12 K·min^{-1}) the sample to base temperature and measured on warming. In addition, time-dependent measurements of the magnetization were performed at 40, 60, and 80 K for up to 3000 min (see Figure S4). These

https://doi.org/10.1021/acs.inorgchem.1c03158
Inorg. Chem. 2021, 60, 19345−19355

measurements were made after rapidly cooling (≈12 K·min^{-1}) the sample from 300 K to the target temperature (where the samples were cooled with the field applied).

Thermal Expansion. Measurements of the macroscopic length change of a crystal of Ag_8SnS_6 were performed using strain gauges. Similar to the design of Kabeya et al.,[42] the full setup used a Wheatstone configuration consisting of two strain gauges and two thin-film resistors. One strain gauge (type FLG-02-23, Tokyo Sokki Kenkyujo Co., Ltd. with R ≈ 120 Ω) was fixed rigidly to the sample by using Devcon 5 min epoxy (No. 14250). The second (identical) strain gauge was fixed to a sample of tungsten carbide, which has a comparatively small thermal expansion coefficient over a wide temperature range, to roughly balance out the intrinsic resistance changes of the strain gauges. In addition, two thin-film resistors with similar and almost temperature-independent absolute resistances of ≈120 Ω were used to complete the Wheatstone bridge. The measured resistance changes were converted into relative length changes using the known gauge factor of the strain gauges (that was assumed to be temperature independent). The cryogenic environment was provided by a closed cycle cryostat (Janis SHI-950 with a base temperature of ≈3.5 K). Temperature control was provided by a LakeShore 336 temperature controller. Helium exchange gas was used to allow for fast cool-down times. The measurements were not aligned along a specific crystallographic direction.

Structure Determination. The crystal structure of Ag_8SnS_6 was determined at 295, 160, and 90 K by single crystal X-ray diffraction. For these measurements, a small, suitable crystal was selected. Single crystal data were collected with a Bruker D8 VENTURE diffractometer (Photon CMOS detector, Mo−IμS microsource, and Oxford Cryosystem 800 lt device). Data integration, absorption correction, and unit cell determination were performed with APEX 3 software. The starting atomic parameters were obtained by direct methods with the SHELXS-2017.[43] Subsequently, the structures were refined using SHELXL-2017 (full-matrix least-squares on F_o^2). Single crystal X-ray diffraction data were first collected at 295 K. Afterward, the sample was slowly cooled to 90 K at a rate of 1 K·min^{-1}, held at 90 K for 30 min, and a full data set was collected at 90 K. The next data sets were collected on heating at 160 and 295 K. In both cases, the crystal was warmed at 6 K·min^{-1} and held at the target temperatures for 30 min prior to collection. Lastly, single crystal data were obtained on a crystal cooled as quickly as possible to 90 K. To accomplish this, the crystal was dismounted and rapidly (a few seconds) mounted back, directly into the nitrogen gas flow, allowing for fast cooling to 90 K.

Variable-Temperature Lattice Parameters. The temperature-dependent lattice constants were determined by tracking the rt orthorhombic $(8\ 0\ 4)_{rt}$, $(0\ 4\ 4)_{rt}$, and $(0\ 0\ 6)_{rt}$ Bragg peaks collected on single crystals. Measurements were performed on a four-circle diffractometer using Cu Kα_1 radiation generated from a rotating anode X-ray source using a germanium (1 1 1) monochromator. Scattered X-rays were measured using an FMB Oxford avalanche pixel diode (APD) single detector system. The sample was mounted on a copper pin using Crystal Bond. The sample was mounted in an ARS 4-800 K He-closed cycle refrigerator. The sample space is sealed with a He exchange gas within the inner Be dome. Two further Be domes were mounted to act as a heat shield and the vacuum shroud. Because during the growth process, the crystals are cooled through a known high-temperature cubic to orthorhombic structural transition that occurs at 460 K,[24] the orthorhombic sample used in this experiment was highly twinned, that is, cryptomorphic. The crystals form with facets perpendicular to the $[1\ 1\ 1]_{PC}$ (PC = pseudocubic) direction which in the rt orthorhombic structure split into the $[2\ 0\ 1]_{rt}$ and $[0\ 1\ 1]_{rt}$ directions. We aligned the crystal within the $[0\ 1\ 1]_{rt}$−$[1\ 1\ 1]_{rt}$ plane, which gives access to a large number of peaks from the available twin domains. Two peaks, the $(8\ 0\ 4)_{rt}$ and $(0\ 4\ 4)_{rt}$, were isolated from other peaks to give a measure of the a and b lattice parameters. The out of plane $(0\ 0\ 6)_{rt}$ peak was measured to determine the c lattice parameter. We first cooled from 300 to 10 K at 0.2 K·min^{-1}. The diffraction data used to determine the lattice parameters were collected by following the evolution of the above peaks on warming at 0.1 K·min^{-1}. The lattice parameters were calculated from the diffraction data using *Bragg's* law and with the rt ($Pna2_1$) unit cell as a basis. Below 120 K, the a and b parameters were transformed into the correct values for the lt phase according to the relationship $2b_{lt} \rightarrow a_{rt}$, in accordance with the relationship between $Pmn2_1$ and $Pna2_1$ space groups.[44]

Computational Methods. Total energies and density of states (DOS) were calculated in density functional theory[45,46] (DFT) with PBEsol[47] exchange-correlation functional, a plane-wave basis set, and projected augmented wave[48] (PAW) method as implemented in VASP.[49,50] A Γ-centered Monkhorst−Pack[51] k-point mesh of (6 × 6 × 4) and (3 × 6 × 4) with a Gaussian smearing of 0.05 eV was used for the lt and rt structures with 30 and 60 atoms in the unit cells, respectively. A kinetic energy cutoff of 323.4 eV was used to fully relax the unit cell and atomic positions until the absolute force on each atom was below 0.02 eV/Å. For bonding and antibonding analysis, the LOBSTER[52] code was used to construct the crystal orbital Hamiltonian population (COHP) for nearest neighbor Ag−S pairs with the bond distance from 2.2 to 3.0 Å.

3. RESULTS AND DISCUSSION

The inset of Figure 1 displays an example of a single crystal grown from the Ag−Sn−S melt. To determine the identity and phase purity of the crystals, we analyzed samples with powder X-ray diffraction at room temperature. Figure 1 shows a representative powder pattern and refinement of the experimental data. The crystals adopt an orthorhombic structure with the $Pna2_1$ space group consistent with the rt phase of Ag_8SnS_6. The refined lattice constants are a = 15.315 5(9) Å, b = 7.553 2(4) Å, c = 10.700 0(6) Å, in agreement with prior reports of Ag_8SnS_6.[23,24,27] The experimental pattern has no observable peaks from secondary phases, supporting successful synthesis of phase-pure materials within the accuracy of our PXRD analysis. Considering the known structural diversity among the broader argyrodite family and the limited lt data on Ag_8SnS_6, we explored the potential for phase transitions in Ag_8SnS_6 below room temperature. We first measured the magnetization of Ag_8SnS_6 between 5−300 K. The temperature-dependent magnetic susceptibility (M/H) is presented in Figure 2a, which shows M/H is negative at all temperatures, indicating diamagnetic behavior, and is consistent with our expectation of Ag_8SnS_6 being a valence precise semiconductor. At high temperatures, M/H has a weak temperature dependence and increases slowly on cooling from -2.6×10^{-4} emu·mol^{-1} at 300 K to -2.55×10^{-4} emu·mol^{-1} at 120 K. The susceptibility data have an abrupt discontinuity at 120 K, falling from -2.55×10^{-4} emu·mol^{-1} to -2.62×10^{-4} emu·mol^{-1}. Given Ag_8SnS_6 is a moderate gap semiconductor with no local moment behavior expected or measured, the clear transition observed in M/H suggests Ag_8SnS_6 undergoes a structural phase transition below ≈120 K.

To provide more detailed characterization of the phase transition, we tracked the thermal expansion of Ag_8SnS_6 between 5 and 300 K. Figure 2b displays the measurement results, given as the magnitude of the temperature-dependent length change normalized to the initial length at room temperature, $[L(T) - L(300\ \text{K})]/L(300\ \text{K})$ (referred to in the text as $\Delta L/L$)). As shown in Figure 2b, the values of $\Delta L/L$ show a rapid and large drop when Ag_8SnS_6 is warmed above 120 K, implying the sample dimensions suddenly contract when this temperature is exceeded. The sudden, jump-like, length change suggests a first-order phase transition, and is characteristic of a structural transformation. The transition temperature closely matches what is observed in the magnetization data, and together the two measurements

https://doi.org/10.1021/acs.inorgchem.1c03158
Inorg. Chem. 2021, 60, 19345−19355

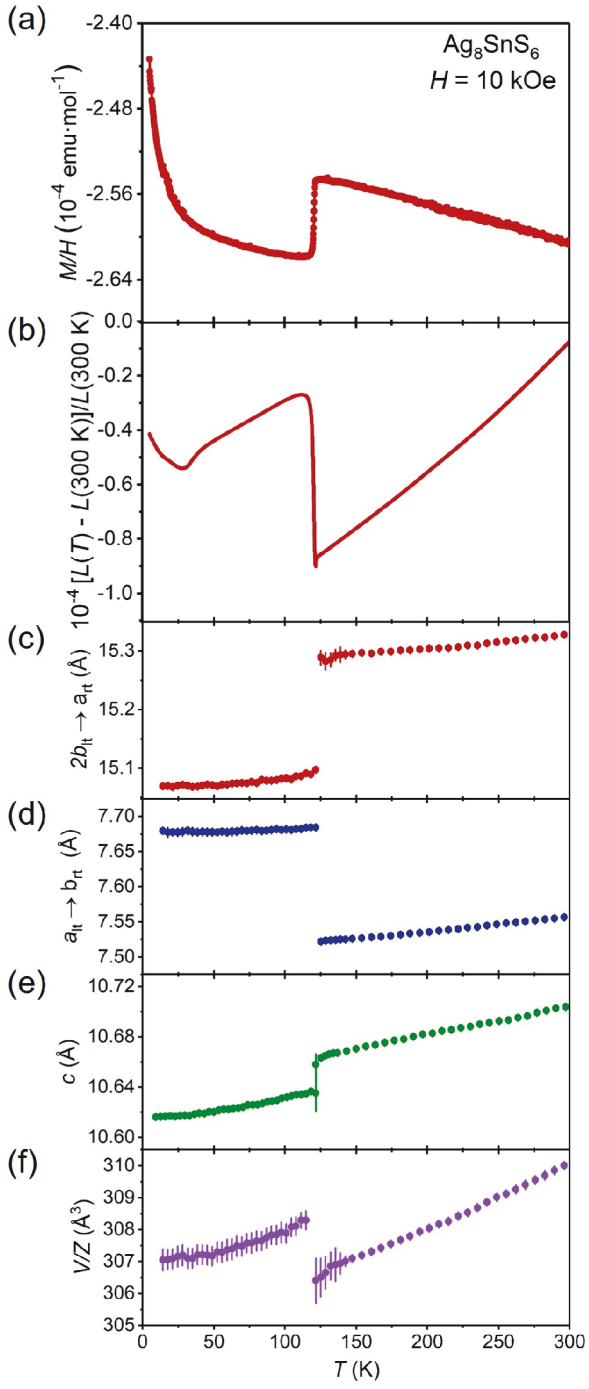

Figure 2. Temperature-dependent physical properties of Ag_8SnS_6 single crystals: (a) magnetic susceptibility (M/H); (b) magnitude of the thermal expansion; (c–e) lattice parameters; and (f) unit cell volume. All data sets were measured on heating.

strongly suggest Ag_8SnS_6 undergoes a first-order structural transition at 120 K. The feature near 30 K in Figure 2b is an artifact caused by the slightly different temperature dependencies of the resistances of the strain gauges (used to determine $\Delta L/L$) at low temperatures.

Having found evidence for a previously unknown structural phase transition in Ag_8SnS_6, we performed single crystal X-ray diffraction at 295, 160, and 90 K to determine the crystal structure of the lt phase. Details regarding the structural refinements are given in the Supporting Information in Table S1, and the crystallographic information regarding the atomic positions, thermal displacement parameters, and individual Ag–S and Sn–S bond lengths are provided in Tables S2–S11. Figure 3 compares the room and lt structures of Ag_8SnS_6 as determined by our single crystal diffraction analysis conducted at 295 and 90 K.

The first data set collected at 295 K agrees with the expected rt orthorhombic unit cell with space group $Pna2_1$ (#33) and a = 15.299 3(9) Å, b = 7.547 9(4) Å, c = 10.704 5(6) Å, and phase volume V/Z = 309.03(3) Å^3, where Z = 4 is the number of formula units per unit cell in the rt structure. These results are consistent with earlier literature.[24,53] The rt structure is complex, as illustrated by Figure 3a,b. All the atoms occupy the Wyckoff position 4a and are labeled respectively as Ag1–Ag8, Sn, and S1–S6. The local environments of the Ag atoms are diverse, with Ag found in distorted tetrahedra (Ag2 and Ag6) as well as trigonal planar (Ag1, Ag3, Ag4, and Ag7) and linear (Ag5) coordination by S. As given in Table S11 of the Supporting Information, the Ag coordination environments are all distorted from the ideal geometries with a wide span of Ag–S bond lengths ranging from 2.4 to 2.69 Å. Each Sn atom is likewise coordinated by a distorted tetrahedron of S atoms with bond lengths of approximately 2.37 Å. The Ag–S and Sn–S tetrahedra form a complicated three-dimensional corner sharing network, with some tetrahedral vertices also linked by the linear and trigonal planar coordinated Ag atoms as shown in Figure 3a,b.

Analysis of the 90 K diffraction data confirms the structural phase transition. We find that at low temperatures, Ag_8SnS_6 adopts a different orthorhombic structure with the space group $Pmn2_1$ (#31) and cell parameters a = 7.662 9(5) Å, b = 7.539 6(5) Å, c = 10.630 0(6) Å, V/Z = 307.08(4) Å^3 (Z = 2 in the lt structure). The lt polymorph of Ag_8SnS_6 is isostructural to the rt forms of the related Se-based argyrodite compounds Ag_8SnSe_6 and Ag_8GeSe_6.[54–56] Several perspectives on the lt variant of Ag_8SnS_6 are illustrated in Figures 3d–f. In the lt polymorph, Ag atoms occupy three 4b and two 2a Wyckoff sites, Sn occupies one 2a Wyckoff site, and S occupies one 4b and four 2a Wyckoff sites. As in the rt phase, there is one Sn atom occupying a distorted tetrahedron of S atoms with bond lengths of approximately 2.38 Å. The lt unit cell contains five unique Ag atoms, three of which (Ag1, Ag2, and Ag5) are found in acentric trigonal planar coordination by sulfur and two (Ag3 and Ag4) that are tetrahedrally coordinated. The Ag–S bond lengths again cover a wide range from 2.44 to 2.79 Å (see Table S10 in the Supporting Information). Unlike the rt phase, the lt structure does not contain Ag atoms in linear coordination.

Notably, $Pna2_1$ (#33) is the maximal non-isomorphic "klassengleich" (class-equivalent) subgroup with index of 2 (k2) of the space group $Pmn2_1$ (#31).[44] Therefore, upon transitioning from the lt to the rt phase on warming, the primitive-orthorhombic cell is retained, but the volume is doubled due to the doubling of the b-lattice parameter, leading to the $Pbn2_1$ space group, which is a non-standard notation for $Pna2_1$. The a and b axis are therefore switched in each polymorph to achieve standard notation for the $Pna2_1$ group. Effectively, moving from the lt to rt structure doubles the unit cell volume, since $a_{rt} \approx 2b_{lt}$. After the transition, each of the 2a sites in the lt structure transform into a single 4a site in the rt structure, while the 4b site in the lt structure becomes two 4a sites in the rt structure. Figure 3 illustrates the relationship between the two structures, showing how each have similar

https://doi.org/10.1021/acs.inorgchem.1c03158
Inorg. Chem. 2021, 60, 19345–19355

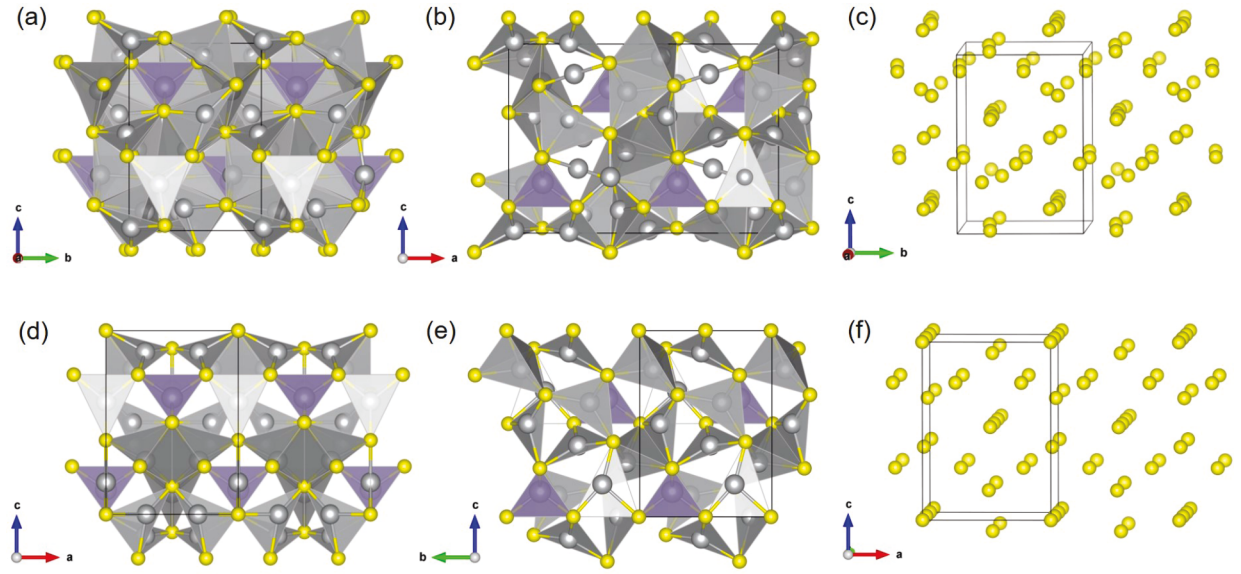

Figure 3. Crystal structure of Ag_8SnS_6 determined at 295 and 90 K. (a–c) 295 K (rt) structure viewed (a) along the *a*-axis and (b) along the *b*-axis. Panel c shows only the S atoms with the perspective titled off the *a*-axis. (d–f) 90 K (lt) structure viewed (d) along the *b*-axis and (b) slightly tilted off the *a*-axis. Panel f shows only the S atoms with the perspective tilted slightly off the *b*-axis. The perspectives in panels c and f emphasize the straightening of the S columns in the lt polymorph. Note that a_{rt} becomes b_{lt}. The color code is as follows: Ag, gray; Sn, purple; S, yellow. The solid black lines denote the unit cell of each structure.

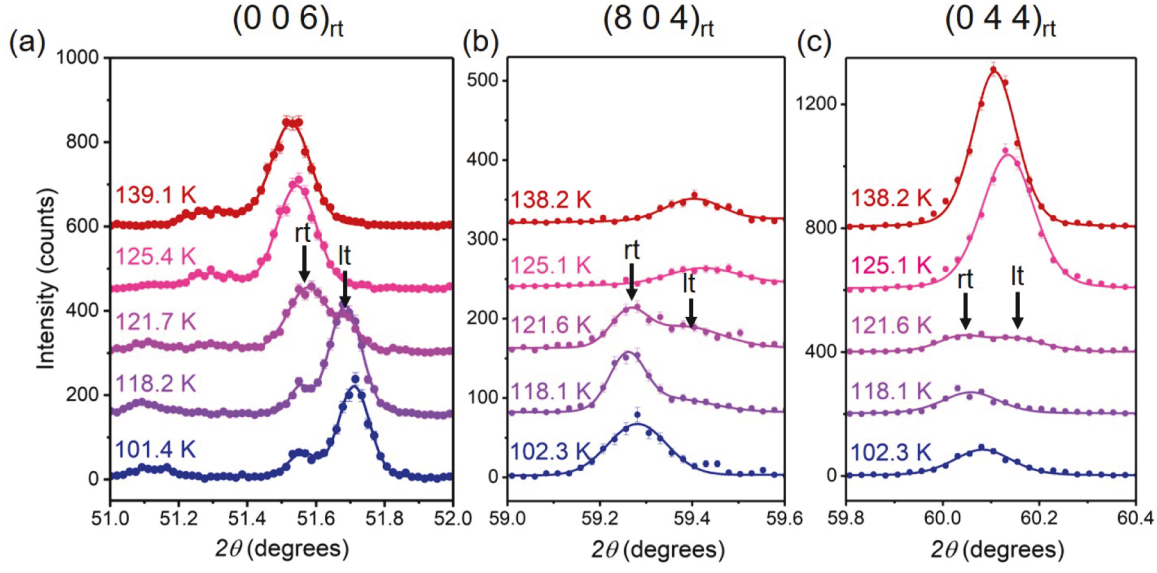

Figure 4. Temperature dependence of the (a) $(0\ 0\ 6)_{rt}$, (b) $(8\ 0\ 4)_{rt}$, and (c) $(0\ 4\ 4)_{rt}$ Bragg peaks of a Ag_8SnS_6 single crystal measured upon warming between ≈100–140 K on a 4-circle diffractometer.

connectivity of atoms, manifested most clearly in the chains/columns of S atoms running down the *a* and *b* axes. We emphasize this in Figure 3 panels c and f by showing only the positions of the S atoms in each polymorph. In the rt phase, the S columns are slightly nonlinear, but in the lt structure the chains straighten such that the S atoms overlay when viewed down the *b*-axis. In this light, the rt structure can be viewed as a distortion of the lt phase, in which the new periodicity resulting from the bending of the S chains doubles the unit cell along the b_{lt} (or a_{rt}) direction. This relationship is somewhat unusual, differing from the more common reduction of symmetry on cooling. Comparing the three polymorphs of Ag_8SnS_6, the crystal structure becomes increasingly distorted as the temperature rises. Starting from the lt $Pmn2_1$ arrangement, the linear S chains become bent on transitioning into the rt $Pna2_1$ structure, and this is accompanied by an increase in the diversity of local coordination environments adopted by the Ag atoms. Finally, the Ag sublattice enters a highly disordered state in the ht cubic phase with high ionic conductivity, where the Ag atoms are distributed over three partially occupied sites.

After determining the lt crystal structure, we next measured the temperature dependence of the lattice parameters by following the rt orthorhombic $(8\ 0\ 4)_{rt}$, $(0\ 4\ 4)_{rt}$, and $(0\ 0\ 6)_{rt}$ diffraction peaks collected on single crystals. Figure 4 shows the evolution of the Bragg peaks on warming in the vicinity of the transition, between ≈100–140 K. Each peak shows sudden changes as the temperature rises above ≈120 K, indicative of the phase change. The $(0\ 0\ 6)_{rt}$ peak shifts to lower 2θ by

https://doi.org/10.1021/acs.inorgchem.1c03158
Inorg. Chem. 2021, 60, 19345–19355

≈0.1°. The $(8\ 0\ 4)_{rt}$ reflection moves to higher 2θ and is significantly reduced in intensity. The $(0\ 4\ 4)_{rt}$ peak moves to higher 2θ and has strongly enhanced intensity. Close inspection of the data collected at ≈120 K shows reflections corresponding to each structure, implying coexistence of both phases across the transition region, which is characteristic of a first-order transformation (the peaks corresponding to each phase are marked by arrows in Figure 4).

Figure 2c–e display the temperature-dependent lattice parameters extracted from the data. The lattice parameters all show abrupt discontinuities at 120 K, consistent with the magnetization and thermal expansion measurements. On warming from the base temperature, the *a*-, *b*-, and *c*-lattice parameters all increase weakly up to approximately 120 K, after which the $2b_{lt}$ expands and becomes a_{rt}, while a_{lt} contracts and becomes b_{rt}. The unit cell dimensions and phase volume all increase gradually with further heating above 120 K. The values at room temperature and 90 K agree with those determined by the single crystal structural refinements discussed above.

An unusual feature of the rt–lt phase transition is that it does not occur in finely ground (powder) samples. Before conducting the X-ray diffraction experiments described above for single crystals, we first attempted to use variable temperature powder XRD to determine the temperature dependence of the lattice parameters. The results of these experiments are presented in Figure S1 in the Supporting Information, and show no evidence for a transition to the $Pmn2_1$ polymorph. Separate magnetization measurements were also conducted on Ag_8SnS_6 powders (Figure S2 in the Supporting Information), and these too provide no evidence of the phase transition. The absence of the rt–lt transition in powdered samples suggests that damage caused by fine grinding (for example dislocation lines, site/antisite disorder, strain, etc.) arrests the transition. Annealing of ground powders (at 170, 250, and 500 °C) did not restore the single crystal behavior in magnetic data (data not shown), suggesting that whatever damage was done by grinding is not readily removed. Whereas fragile magnetic phase transitions,[57] for example, such as those found for YbPtBi,[58] are known to be susceptible to strain of small structural perturbations, it is uncommon to have a 100 K, structural phase transition exhibit such sensitivity to damage induced by fine grinding. Ultimately, while the absence of the transition is anomalous, detailed investigation of this phenomenon is outside the intended scope of this manuscript.

Given that the transition is structural and appears to be first-order in nature, we also collected magnetization and thermal expansion data upon heating and cooling. The magnetic data are shown in Figure 5a, demonstrating large hysteresis in M/H between heating and cooling at 0.5 K·min^{-1}. Comparable hysteresis is also detected in the thermal expansion data, as displayed in Figure 5b. Since the extent of the hysteresis can depend on the rate of temperature change, we quenched our samples (i.e., cooled as rapidly as possible to 5 K) and then measured upon slowly warming. For both magnetization and thermal expansion measurements, the trend from 5 to 60 K (after quenching) appears to match a rough extrapolation of the 130–300 K data to lower temperatures. As the sample is heated above 60 K, both magnetization and thermal expansion data sets show a clear drop followed by a rapid increase on warming at 120 K. These results imply that fast cooling traps the crystal in the rt phase. The metastable state is maintained

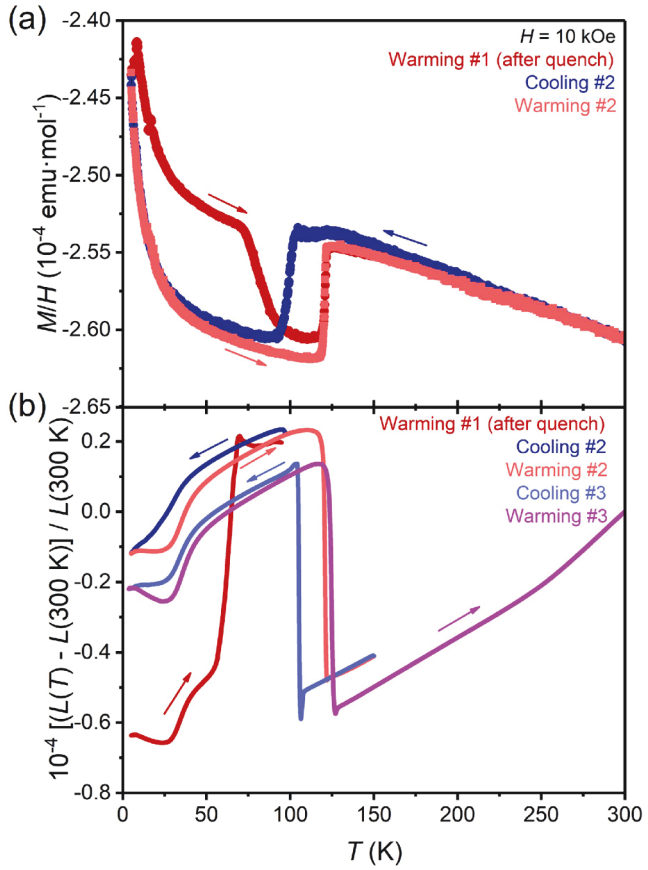

Figure 5. Thermal hysteresis of the structural transition in Ag_8SnS_6. (a) Temperature-dependent magnetic susceptibility and (b) thermal expansion. See text for details about quenching.

upon slow warming until about 60–70 K, where both the M/H and $\Delta L/L$ data return to the slow heating/cooling manifold.

We furthermore measured the thermal expansion with different heating and cooling rates. The results are presented in Figure S3 in the Supporting Information, and indicate cooling at a rate faster than 4–5 K/min is sufficient to arrest the crystallographic transformation. On warming, a clear transition to the lt polymorph begins at ≈60 K, and this transformation is relatively insensitive to the heating rate. Given that the metastable state appears to be preserved below 60 K, we last tracked the magnetic susceptibility over time at T = 40, 60, and 80 K to determine how quickly the thermodynamically stable lt variant is recovered after quenching to each temperature. Figure S4 in the Supporting Information shows the results. We find that the transition into the lt polymorph begins almost immediately at 80 K, takes 100s of minutes to become noticeable at 60 K, and remains in the metastable rt phase for the duration of our 1000 min measurement at 40 K.

The lt–rt phase transition can be considered as a reconstructive phase transition;[59,60] for example, chemical bonds are broken and reformed. Such transitions involve considerable atomic motions and are always first-order with hysteresis. The hysteresis can be understood as a case of kinetic arrest,[61] caused by the competition between the Gibbs free energy (the transformation driving force), the strain energy (transformation opposing force), and the thermal energy that allows for atomic rearrangement. Our thermal expansion and magnetization data suggest the thermal energy below at least 40 K is insufficient to drive the structural

https://doi.org/10.1021/acs.inorgchem.1c03158
Inorg. Chem. 2021, 60, 19345–19355

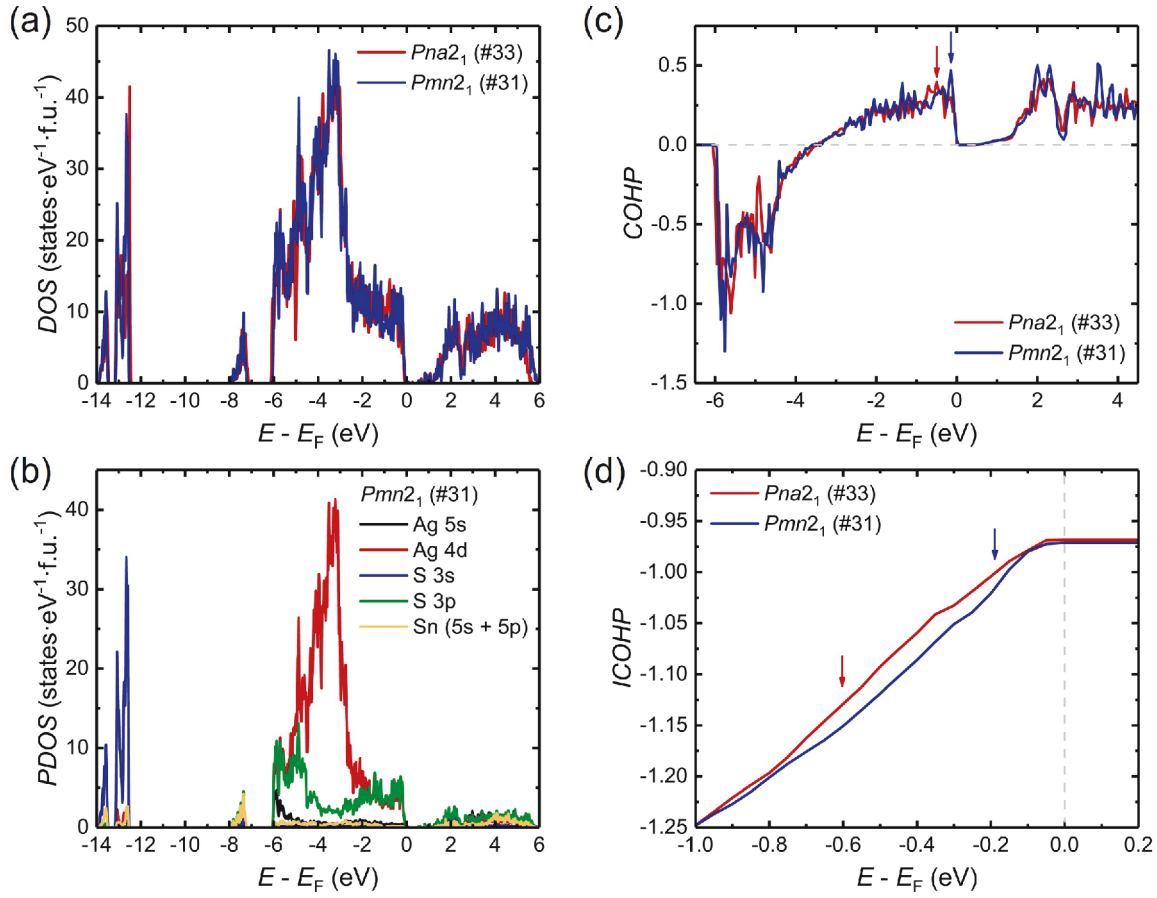

Figure 6. (a) DFT calculated density of states for Ag_8SnS_6 in the rt ($Pna2_1$) and lt ($Pmn2_1$) structure. (b) Orbital projected density of states for Ag_8SnS_6 in the lt structure. (c) Crystal orbital Hamiltonian population (COHP) plots for nearest neighbor Ag−S interactions in Ag_8SnS_6 for the rt and lt structures. (d) Integrated COHP for each structure. The arrows in panels c and d mark the positions of relevant antibonding COHP peaks that shift to higher energy in the lt structure.

rearrangement to the lt polymorph, allowing for the sample to be arrested in the rt structure by rapid cooling. On warming the quenched sample, the structure transforms to the thermodynamically favored lt structure when the thermal energy overcomes the activation barrier. These results suggest that Ag_8SnS_6 may serve as a model system for the study of time−temperature−phase relations associated with a quenchable, structural phase transition. The advantages of Ag_8SnS_6 are (i) it is a stoichiometric phase that can be grown in high purity form and (ii) the transition from one phase to another can be monitored by a contact-free measurement such as magnetization.

Although we were not able to perform single crystal X-ray diffraction studies below 90 K, that is, we could not reach the quenched, metastable rt structure that exists for long periods of time below 40 K, we could still directly compare the two orthorhombic structures (rt and lt versions) at the same temperature by taking advantage of the hysteresis of the phase transition (i.e., in the 90−125 K region in Figure 5). Given that the width of the hysteresis depends on cooling rate (Figure S3), we cooled a sample as rapidly as possible to 90 K and collected single crystal diffraction data (see the experimental section for more details). After fast cooling, the diffraction data revealed an orthorhombic $Pna2_1$ unit cell (a = 15.272 4(9) Å, b = 7.519 7(5) Å, c = 10.656 9(7) Å, V/Z = 305.98(3) Å^3), consistent with rt Ag_8SnS_6. The quickly cooled, 90 K, results are in qualitative agreement with the behavior of the lattice parameters shown in Figure 2c−f. Table S11 in the Supporting Information compares Sn−S and Ag−S bond lengths determined by the single crystal data at each temperature, and we find that at 90 K, most bonds are slightly longer in the lt variant than in the 90 K rt $Pna2_1$ arrangement, consistent with the larger V/Z of the lt structure.

Like rt Ag_8SnS_6, the related argyrodite compounds Ag_8GeS_6 and Ag_8SiS_6 both adopt the $Pna2_1$ structure,[62,63] whereas Ag_8SnSe_6 and Ag_8GeSe_6 take the $Pmn2_1$ form.[54−56] From this information, we observe a trend relating the unit cell dimensions (normalized to Z) to the preferred structure of each material. Owing to the smaller size of Ge and Si compared to Sn, Ag_8GeS_6 and Ag_8SiS_6 have smaller respective phase volumes of 299 and 296 Å^3 compared to 309 Å^3 for Ag_8SnS_6. Similarly, Se is larger than S, and Ag_8GeSe_6 and Ag_8SnSe_6 both have larger V/Z of 328 and 342 Å^3, respectively. The preferred structures indicate that increasing V/Z favors the $Pmn2_1$ arrangement. This reasoning is consistent with the intermediate V/Z of Ag_8SnS_6 and the observation of both polymorphs in this compound.

To support this argument based on crystallography, we used DFT to compare the calculated formation energies of Ag_8SnS_6 and Ag_8GeS_6 in both $Pna2_1$ and $Pmn2_1$ structures at zero temperature. With the PBEsol exchange-correlation functional, the fully relaxed lattice parameters for Ag_8SnS_6 are a = 15.03 Å, b = 7.40 Å, and c = 10.58 Å for the rt structure, and a = 7.63 Å, b = 7.42 Å, and c = 10.49 Å for the lt structure. Both relaxed

https://doi.org/10.1021/acs.inorgchem.1c03158
Inorg. Chem. 2021, 60, 19345−19355

lattice parameters are within 2% and smaller than the experimental data, which is typically acceptable for PBEsol. The corresponding total energy difference (ΔE) favors the lt structure by 0.14 eV·f.u.$^{-1}$ (or 9.5 meV·atom^{-1}), agreeing with the experimental observation of the $Pmn2_1$ variant being the ground state structure. For Ag_8GeS_6, the calculations indicate the $Pmn2_1$ structure is also more stable, but by only 2.9 meV·atom^{-1}. We note that the calculated ΔE is only weakly affected by the inclusion of spin−orbit coupling (SOC), changing to 9.7 meV·atom^{-1} for Ag_8SnS_6. Thus, the following results are all from DFT calculations without SOC.

The calculations are qualitatively consistent with our suggestion that the $Pmn2_1$ structure is favored to a greater degree for larger phase volume. This implies that applying pressure to Ag_8SnS_6, or contracting the lattice, should suppress the transition temperature. We tested this by applying chemical pressure through isovalent alloying with the smaller Ge in place of Sn. We prepared single crystals of $Ag_8Sn_{1-x}Ge_xS_6$ (nominal x = 0.10, 0.25) and pure Ag_8GeS_6 following the same growth procedure used for the Ag_8SnS_6. Powder X-ray diffraction analysis indicates successful Ge incorporation (Figures S4 and S5). The lattice parameters decrease monotonically moving from Ag_8SnS_6 to Ag_8GeS_6 with a greater slope than anticipated by Vegard's law, which may suggest the samples are enriched with Ge with respect to the nominal compositions. Magnetization data measured from 5 to 300 K is given in Figure S7, and we find no evidence for a phase transition in any of the Ge containing samples. Although we cannot definitively rule out a disorder broadened transition, the magnetization data support the arguments presented here, and indicate that the lattice contraction caused by even a relatively small (≈ 10%) addition of Ge is sufficient to eliminate the transition. Suppression of the transition after lattice contraction is likewise consistent with our X-ray analysis, which showed an increase in V/Z when cooling through the transition. In principle, our arguments could be further tested by expanding the lattice with "negative pressure" or alloying with larger atoms, which we anticipate would raise the transition temperature of Ag_8SnS_6. Likewise, we predict that applying pressure to Ag_8GeSe_6 may stabilize a currently unreported $Pna2_1$ polymorph.

Our calculations and experimental results indicate the preferred structure of the argyrodite members is closely related to the normalized unit cell volume. This observation is likely grounded in the different strengths of the chemical bonding in each material, which will naturally be reflected in the bond lengths. The structures adopted by the various argyrodite materials, along with the experiments and calculations presented here, suggest that larger volume (longer bonds) favors the $Pmn2_1$ variant. Because the local tetrahedral coordination environment around Sn remains essentially unchanged in each phase, whereas the changes to the Ag−S sublattice are more significant, we anticipate the Ag−S interactions are most important in determining the preferred structure.

To provide more insight into the role of chemical bonding in determining the relative stability for the two Ag_8SnS_6 structures, we also used DFT to calculate the density of states (DOS) and crystal orbital Hamilton population (COHP) for each polymorph. Figure 6a shows the calculated total DOS for each structure of Ag_8SnS_6, and Figure 6b displays the atomic orbital projected density of states (PDOS) for the lt structure to show the positions of the relevant bands. The overall DOS for each structure are very similar. The states from −14 to −12 eV are mostly from the S 3s orbitals, and those from −8 to −7 eV are primarily from Sn 5s orbitals, respectively. The Sn 5p bands (plotted together with Sn 5s) spread out in a broad energy range above −6 eV and have low magnitude due to the small number of Sn atoms. The Ag 4d bands range from −6 and 0 eV, with the main peak centered around −3.5 eV. The Ag 5s bands spread from −6 eV to the conduction band, with the greatest contribution being from −6 to −5.5 eV, where they overlap with the lower edge of the Ag 4d bands. The S 3p bands range from −8 eV to the conduction band with two regions of greatest contribution, one from −6 to −4.5 eV and the other from −2 to 0 eV.

The COHP for nearest-neighbor Ag−S pairs is presented in Figure 6c. COHP decomposes the density of states into nearest neighbor pair interactions and gives information on bonding and antibonding contributions to the band structure energy,[64] respectively denoted by negative (stabilizing) and positive (destabilizing) COHP values. The COHP plot clearly shows that the Ag−S band hybridization from −6 to −3.4 eV gives bonding states and that the states above −3.4 eV are antibonding. The relative stability of the two structures depends on the details of how the states in these bonding and antibonding regions distribute differently, which reflects the rearrangements of Ag−S local coordination and the different bond lengths in each structure. In the bonding region, the primary COHP peaks reach more negative values in the lt structure. Likewise, in the antibonding region, the most notable change is the shift of the COHP peak from −0.6 to −0.2 eV as indicated by the two vertical arrows in Figure 6c. The effects of these changes on the overall stability are captured by integrating the COHP (ICOHP) to the Fermi level, which gives the contribution from the nearest neighbor Ag−S pairs to the total energy. As shown in Figure 6d and zoomed just below the Fermi energy E_F, after integrating up to E_F, we ultimately find the lt arrangement to be more stable than the rt structure by 2 meV/pair, in qualitative agreement with our overall DFT energy calculations discussed earlier. The calculations therefore indicate that differences in the Ag−S bonding significantly impact the energetically favored structure.

4. SUMMARY AND CONCLUSIONS

We grew single crystals of the semiconducting mineral Ag_8SnS_6 from a Ag−Sn−S melt. Temperature-dependent magnetization, thermal expansion, and X-ray diffraction measurements demonstrate Ag_8SnS_6 crystals undergo a structural transition from the rt ($Pna2_1$) form to a different orthorhombic ($Pmn2_1$) structure below 120 K (on warming). The lt polymorph is isostructural to the related argyrodites Ag_8SnSe_6 and Ag_8GeSe_6. We find the transition temperature to be strongly dependent on the cooling rate, and samples rapidly quenched at speeds faster than ≈4−5 K·min^{-1} can be trapped in a metastable form of the rt phase for temperatures up to at least 40 K. As such, Ag_8SnS_6 may serve as a model system for the study of time−temperature−phase relations associated with a quenchable, structural phase transition. On the basis of the structures preferred by each family of argyrodite materials Ag_8TQ_6 (T = Si, Ge, Sn; Q = S, Se), we suggest that lower volumes (per formula unit) increasingly favor the $Pna2_1$ variant. We support this picture by applying chemical pressure to Ag_8SnS_6 by alloying with Ge to form $Ag_8Sn_{1-x}Ge_xS_6$, and find that a small lattice contraction from 10% incorporation of Ge is sufficient

https://doi.org/10.1021/acs.inorgchem.1c03158
Inorg. Chem. 2021, 60, 19345−19355

to avoid the lt-rt phase change in $Ag_8Sn_{1-x}Ge_xS_6$. We last use density function theory calculations to suggest that differences in Ag−S bonding determine the energetically preferred structure.

■ ASSOCIATED CONTENT

Supporting Information

. The Supporting Information is available free of charge at https://pubs.acs.org/doi/10.1021/acs.inorgchem.1c03158.

Variable temperature powder X-ray diffraction; magnetization measurements on powdered samples; thermal expansion measurements conducted with different warming/cooling rates; time-dependent magnetization at 40, 60, and 80 K; powder X-ray diffraction of Ge alloyed samples; magnetic susceptibility of Ge alloyed samples; tables of crystallographic data (PDF)

Accession Codes

CCDC 2105238 and 2105240−2105242 contain the supplementary crystallographic data for this paper. These data can be obtained free of charge via www.ccdc.cam.ac.uk/data_request/cif, or by emailing data_request@ccdc.cam.ac.uk, or by contacting The Cambridge Crystallographic Data Centre, 12 Union Road, Cambridge CB2 1EZ, UK; fax: +44 1223 336033.

■ AUTHOR INFORMATION

Corresponding Authors

Tyler J. Slade − *Ames Laboratory, US DOE, Iowa State University, Ames, Iowa 50011, United States; Department of Physics and Astronomy, Iowa State University, Ames, Iowa 50011, United States;* orcid.org/0000-0001-6751-4303; Email: slade@ameslab.gov

Paul C. Canfield − *Ames Laboratory, US DOE, Iowa State University, Ames, Iowa 50011, United States; Department of Physics and Astronomy, Iowa State University, Ames, Iowa 50011, United States*; Email: canfield@ameslab.gov

Authors

Volodymyr Gvozdetskyi − *Department of Chemistry, Iowa State University, Ames, Iowa 50011, United States*

John M. Wilde − *Ames Laboratory, US DOE, Iowa State University, Ames, Iowa 50011, United States; Department of Physics and Astronomy, Iowa State University, Ames, Iowa 50011, United States*

Andreas Kreyssig − *Ames Laboratory, US DOE, Iowa State University, Ames, Iowa 50011, United States; Department of Physics and Astronomy, Iowa State University, Ames, Iowa 50011, United States*

Elena Gati − *Ames Laboratory, US DOE, Iowa State University, Ames, Iowa 50011, United States; Department of Physics and Astronomy, Iowa State University, Ames, Iowa 50011, United States*

Lin-Lin Wang − *Ames Laboratory, US DOE, Iowa State University, Ames, Iowa 50011, United States; Department of Physics and Astronomy, Iowa State University, Ames, Iowa 50011, United States;* orcid.org/0000-0003-0965-3246

Yaroslav Mudryk − *Ames Laboratory, US DOE, Iowa State University, Ames, Iowa 50011, United States;* orcid.org/0000-0003-2658-0413

Raquel A. Ribeiro − *Ames Laboratory, US DOE, Iowa State University, Ames, Iowa 50011, United States; Department of Physics and Astronomy, Iowa State University, Ames, Iowa 50011, United States*

Vitalij K. Pecharsky − *Ames Laboratory, US DOE, Iowa State University, Ames, Iowa 50011, United States; Department of Materials Science and Engineering, Iowa State University, Ames, Iowa 50011, United States*

Julia V. Zaikina − *Department of Chemistry, Iowa State University, Ames, Iowa 50011, United States;* orcid.org/0000-0002-8755-1926

Sergey L. Bud'ko − *Ames Laboratory, US DOE, Iowa State University, Ames, Iowa 50011, United States; Department of Physics and Astronomy, Iowa State University, Ames, Iowa 50011, United States*

Complete contact information is available at: https://pubs.acs.org/10.1021/acs.inorgchem.1c03158

Notes

The authors declare no competing financial interest.

■ ACKNOWLEDGMENTS

Work at the Ames Laboratory (T.J.S., J.M.W., A.K., E.G., L.W., R.A.R., Y.M., V.K.P., S.L.B., P.C.C.) was supported by the U.S. Department of Energy, Office of Science, Basic Energy Sciences, Materials Sciences and Engineering Division. The Ames Laboratory is operated for the U.S. Department of Energy by Iowa State University under Contract No. DE-AC02-07CH11358. T.J.S. was supported by the Center for Advancement of Topological Semimetals (CATS), an Energy Frontier Research Center funded by the U.S. Department of Energy Office of Science, Office of Basic Energy Sciences, through the Ames Laboratory under its Contract No. DE-AC02-07CH11358 with Iowa State University. T.J.S. and E.G. also acknowledge funding from the Gordon and Betty Moore Foundation's EPiQS Initiative through Grant No. GBMF4411. J.V.Z. acknowledges financial support from the National Science Foundation (DMR-1944551). Temperature-dependent powder diffraction experiments (Y.M., V.K.P.) were supported by the Division of Materials Science and Engineering of the Office of Basic Energy Sciences. Earlier attempts to grow and study single crystal Ag_8SnS_6 samples were made by X. Lin, W. Meier, and G. Drachuck. P.C.C. acknowledges D. Argyriou for geologic reasons. The authors thank Tom Lograsso and Matt Kramer for useful discussions.

■ REFERENCES

(1) Wiegers, G. The crystal structure of the low-temperature form of silver selenide. *American Mineralogist: Journal of Earth and Planetary Materials* **1971**, *56*, 1882−1888.

(2) Kuhs, W.; Nitsche, R.; Scheunemann, K. The argyrodites-A new family of tetrahedrally close-packed structures. *Mater. Res. Bull.* **1979**, *14*, 241−248.

(3) Wood, P. T.; Pennington, W. T.; Kolis, J. W. Synthesis of novel solid-state compounds in supercritical solvents: preparation and structure of $K_2Ag_{12}Se_7$ in supercritical ethylenediamine. *J. Am. Chem. Soc.* **1992**, *114*, 9233−9235.

(4) Li, J.; Guo, H.-Y.; Zhang, X.; Kanatzidis, M. G. $CsAg_5Te_3$: a new metal-rich telluride with a unique tunnel structure. *J. Alloys Compd.* **1995**, *218*, 1−4.

(5) Yakshibayev, R.; Almukhametov, R.; Balapanov, M. K. Ionic conductivity and chemical diffusion in Ag_2Se Cu_2Se mixed conductor compounds. *Solid State Ionics* **1989**, *31*, 247−251.

(6) Junod, P.; Hediger, H.; Kilchör, B.; Wullschleger, J. Metal-non-metal transition in silver chalcogenides. *Philos. Mag.* **1977**, *36*, 941−958.

(7) Boyce, J. B.; Huberman, B. A. Superionic conductors: Transitions, structures, dynamics. *Phys. Rep.* **1979**, *51*, 189−265.

(8) Rettie, A. J.; Malliakas, C. D.; Botana, A. S.; Hodges, J. M.; Han, F.; Huang, R.; Chung, D. Y.; Kanatzidis, M. G. Ag_2Se to KAg_3Se_2: Suppressing Order−Disorder Transitions via Reduced Dimensionality. *J. Am. Chem. Soc.* **2018**, *140*, 9193−9202.
(9) Morelli, D.; Jovovic, V.; Heremans, J. Intrinsically minimal thermal conductivity in cubic I- V-VI_2 semiconductors. *Phys. Rev. Lett.* **2008**, *101*, 035901.
(10) Roychowdhury, S.; Ghosh, T.; Arora, R.; Samanta, M.; Xie, L.; Singh, N. K.; Soni, A.; He, J.; Waghmare, U. V.; Biswas, K. Enhanced atomic ordering leads to high thermoelectric performance in $AgSbTe_2$. *Science* **2021**, *371*, 722−727.
(11) Lin, H.; Tan, G.; Shen, J.-N.; Hao, S.; Wu, L.-M.; Calta, N.; Malliakas, C.; Wang, S.; Uher, C.; Wolverton, C.; Kanatzidis, M. G. Concerted rattling in $CsAg_5Te_3$ leading to ultralow thermal conductivity and high thermoelectric performance. *Angew. Chem.* **2016**, *128*, 11603−11608.
(12) Kim, J.-H.; Chung, D.-Y.; Bilc, D.; Loo, S.; Short, J.; Mahanti, S. D.; Hogan, T.; Kanatzidis, M. G. Crystal Growth, Thermoelectric Properties, and Electronic Structure of $AgBi_3S_5$ and $AgSb_xBi_{3-x}S_5$ (x= 0.3). *Chem. Mater.* **2005**, *17*, 3606−3614.
(13) Charoenphakdee, A.; Kurosaki, K.; Muta, H.; Uno, M.; Yamanaka, S. Ag_8SiTe_6: a new thermoelectric material with low thermal conductivity. *Jpn. J. Appl. Phys.* **2009**, *48*, 011603.
(14) Acharya, S.; Pandey, J.; Soni, A. Enhancement of Power Factor for Inherently Poor Thermal Conductor Ag_8GeSe_6 by Replacing Ge with Sn. *ACS Applied Energy Materials* **2019**, *2*, 654−660.
(15) Lin, S.; Li, W.; Pei, Y. Thermally insulative thermoelectric argyrodites. *Mater. Today* **2021**, *48*, 198.
(16) Zeier, W. G.; Zevalkink, A.; Gibbs, Z. M.; Hautier, G.; Kanatzidis, M. G.; Snyder, G. J. Thinking like a chemist: intuition in thermoelectric materials. *Angew. Chem., Int. Ed.* **2016**, *55*, 6826−6841.
(17) Stroyuk, O.; Raevskaya, A.; Gaponik, N. Solar light harvesting with multinary metal chalcogenide nanocrystals. *Chem. Soc. Rev.* **2018**, *47*, 5354−5422.
(18) Lin, X.; Bud'ko, S. L.; Canfield, P. C. Development of viable solutions for the synthesis of sulfur bearing single crystals. *Philos. Mag.* **2012**, *92*, 2436−2447.
(19) Kanatzidis, M. G. Discovery-synthesis, design, and prediction of chalcogenide phases. *Inorg. Chem.* **2017**, *56*, 3158−3173.
(20) Kanatzidis, M. G. New directions in synthetic solid state chemistry: chalcophosphate salt fluxes for discovery of new multinary solids. *Curr. Opin. Solid State Mater. Sci.* **1997**, *2*, 139−149.
(21) Kanatzidis, M. G. Molten alkali-metal polychalcogenides as reagents and solvents for the synthesis of new chalcogenide materials. *Chem. Mater.* **1990**, *2*, 353−363.
(22) Palache, C. Memorial of Frederick Alexander Canfield. *Am. Miner.: J. Earth Planet. Mater.* **1927**, *12*, 67−70.
(23) Mikolaichuk, A.; Moroz, N.; Demchenko, P. Y.; Akselrud, L.; Gladyshevskii, R. Phase relations in the Ag_8SnS_6-Ag_2SnS_3-AgBr system and crystal structure of $Ag_6SnS_4Br_2$. *Inorg. Mater.* **2010**, *46*, 590−597.
(24) Shen, X.; Xia, Y.; Yang, C.-C.; Zhang, Z.; Li, S.; Tung, Y.-H.; Benton, A.; Zhang, X.; Lu, X.; Wang, G.; He, J.; Zhou, X. High Thermoelectric Performance in Sulfide-Type Argyrodites Compound $Ag_8Sn(S_{1-x}Se_x)_6$ Enabled by Ultralow Lattice Thermal Conductivity and Extended Cubic Phase Regime. *Adv. Funct. Mater.* **2020**, *30*, 2000526.
(25) Ghrib, T.; Al-Otaibi, A. L.; Almessiere, M. A.; Assaker, I. B.; Chtourou, R. High Thermoelectric Figure of Merit of Ag_8SnS_6 Component Prepared by Electrodeposition Technique. *Chin. Phys. Lett.* **2015**, *32*, 127402.
(26) An, C.; Tang, K.; Shen, G.; Wang, C.; Huang, L.; Qian, Y. The synthesis and characterization of nanocrystalline Cu-and Ag-based multinary sulfide semiconductors. *Mater. Res. Bull.* **2003**, *38*, 823−830.
(27) Li, B.; Xie, Y.; Huang, J.; Su, H.; Qian, Y. Synthesis and characterization of ternary chalcogenides Ag_8SnE_6 (E = S, Se). *J. Solid State Chem.* **2000**, *149*, 338−340.
(28) Li, Q.; Ding, Y.; Liu, X.; Qian, Y. Preparation of ternary I-IV-VI nanocrystallines via a mild solution route. *Mater. Res. Bull.* **2001**, *36*, 2649−2656.
(29) He, Q.; Huang, S.; Wang, C.; Qiao, Q.; Liang, N.; Xu, M.; Chen, W.; Zai, J.; Qian, X. The role of Mott−Schottky heterojunctions in Ag−Ag_8SnS_6 as counter electrodes in dye-sensitized solar cells. *ChemSusChem* **2015**, *8*, 817−820.
(30) Cheng, K.-W.; Tsai, W.-T.; Wu, Y.-H. Photo-enhanced salt-water splitting using orthorhombic Ag_8SnS_6 photoelectrodes in photoelectrochemical cells. *J. Power Sources* **2016**, *317*, 81−92.
(31) Shambharkar, B. H.; Chowdhury, A. P. Ethylene glycol mediated synthesis of Ag_8SnS_6 nanoparticles and their exploitation in the degradation of eosin yellow and brilliant green. *RSC Adv.* **2016**, *6*, 10513−10519.
(32) Lu, C.-L.; Zhang, L.; Zhang, Y.-W.; Liu, S.-Y.; Mei, Y. Electronic, optical properties, surface energies and work functions of Ag_8SnS_6: First-principles method. *Chin. Phys. B* **2015**, *24*, 017501.
(33) Zhu, L.; Xu, Y.; Zheng, H.; Liu, G.; Xu, X.; Pan, X.; Dai, S. Application of facile solution-processed ternary sulfide Ag_8SnS_6 as light absorber in thin film solar cells. *Science China Materials* **2018**, *61*, 1549−1556.
(34) Boon-on, P.; Aragaw, B. A.; Lee, C.-Y.; Shi, J.-B.; Lee, M.-W. Ag_8SnS_6: a new IR solar absorber material with a near optimal bandgap. *RSC Adv.* **2018**, *8*, 39470−39476.
(35) Sharma, R.; Chang, Y. The Ag-S (Silver-Sulfur) system. *Bull. Alloy Phase Diagrams* **1986**, *7*, 263−269.
(36) Sharma, R.; Chang, Y. The S-Sn (sulfur-tin) system. *Bull. Alloy Phase Diagrams* **1986**, *7*, 269−273.
(37) Okamoto, H. *Phase diagrams for binary alloys*; ASM International, 2010; Vol. *44*.
(38) Wang, N.; Fan, A. An experimental study of the Ag_2S-SnS_2 pseudobinary join. *Neues Jahrbuch für Mineralogie* **1989**, *160*, 33−36.
(39) Canfield, P. C.; Kong, T.; Kaluarachchi, U. S.; Jo, N. H. Use of frit-disc crucibles for routine and exploratory solution growth of single crystalline samples. *Philos. Mag.* **2016**, *96*, 84−92.
(40) Canfield, P. C. New materials physics. *Rep. Prog. Phys.* **2020**, *83*, 016501.
(41) Toby, B. H.; Von Dreele, R. B. GSAS-II: the genesis of a modern open-source all purpose crystallography software package. *J. Appl. Crystallogr.* **2013**, *46*, 544−549.
(42) Kabeya, N.; Imura, K.; Deguchi, K.; K. Sato, N. Thermal Expansion Measurements Using the Strain Gauge Technique with Kelvin Double Bridge. *J. Phys. Soc. Jpn.* **2011**, *80*, SA098.
(43) Sheldrick, G. M. A short history of SHELX. *Acta Crystallogr., Sect. A: Found. Crystallogr.* **2008**, *64*, 112−122.
(44) Hahn, T. *International Tables for Crystallography*; International Union of Crystallography, Vol. *I*, DOI: 10.1107/97809553602060000001.
(45) Hohenberg, P.; Kohn, W. Inhomogeneous electron gas. *Phys. Rev.* **1964**, *136*, B864.
(46) Kohn, W.; Sham, L. J. Self-consistent equations including exchange and correlation effects. *Phys. Rev.* **1965**, *140*, A1133.
(47) Perdew, J. P.; Ruzsinszky, A.; Csonka, G. I.; Vydrov, O. A.; Scuseria, G. E.; Constantin, L. A.; Zhou, X.; Burke, K. Restoring the density-gradient expansion for exchange in solids and surfaces. *Phys. Rev. Lett.* **2008**, *100*, 136406.
(48) Blöchl, P. E. Projector augmented-wave method. *Phys. Rev. B: Condens. Matter Mater. Phys.* **1994**, *50*, 17953.
(49) Kresse, G.; Furthmüller, J. Efficient iterative schemes for ab initio total-energy calculations using a plane-wave basis set. *Phys. Rev. B: Condens. Matter Mater. Phys.* **1996**, *54*, 11169.
(50) Kresse, G.; Furthmüller, J. Efficiency of ab-initio total energy calculations for metals and semiconductors using a plane-wave basis set. *Comput. Mater. Sci.* **1996**, *6*, 15−50.
(51) Monkhorst, H. J.; Pack, J. D. Special points for Brillouin-zone integrations. *Phys. Rev. B* **1976**, *13*, 5188.
(52) Maintz, S.; Deringer, V. L.; Tchougréeff, A. L.; Dronskowski, R. Analytic projection from plane-wave and PAW wavefunctions and

application to chemical-bonding analysis in solids. *J. Comput. Chem.* **2013**, *34*, 2557−2567.
(53) Wang, N. New Data for Ag_8SnS_6 (Canfieldite) and Ag_8GeS_6 (Argyrodite). *Neues Jahrbuch für Mineralogie* **1978**, 269−272.
(54) Gulay, L.; Olekseyuk, I.; Parasyuk, O. Crystal structure of *β*-Ag_8SnSe_6. *J. Alloys Compd.* **2002**, *339*, 113−117.
(55) Semkiv, I.; Ilchuk, H.; Pawlowski, M.; Kusnezh, V. Ag_8SnSe_6 argyrodite synthesis and optical properties. *Opto-Electron. Rev.* **2017**, *25*, 37−40.
(56) Carre, D.; Ollitrault-Fichet, R.; Flahaut, J. Structure de Ag_8GeSe_6 *β*. *Acta Crystallogr., Sect. B: Struct. Crystallogr. Cryst. Chem.* **1980**, *36*, 245−249.
(57) Canfield, P. C.; Bud'ko, S. L. Preserved entropy and fragile magnetism. *Rep. Prog. Phys.* **2016**, *79*, 084506.
(58) Mun, E.; Bud'ko, S. L.; Martin, C.; Kim, H.; Tanatar, M. A.; Park, J.-H.; Murphy, T.; Schmiedeshoff, G.; Dilley, N.; Prozorov, R.; Canfield, C. Paul Magnetic-field-tuned quantum criticality of the heavy-fermion system YbPtBi. *Phys. Rev. B: Condens. Matter Mater. Phys.* **2013**, *87*, 075120.
(59) Buerger, M. Polymorphism and phase transformations. *Fortschr. Mineral* **1961**, *39*.
(60) Buerger, M. J. *Phase Transformations in Solids*; Wiley: New York, 1951; Chapter 6.
(61) Chattopadhyay, M.; Roy, S.; Chaddah, P. Kinetic arrest of the first-order ferromagnetic-to-antiferromagnetic transition in Ce $(Fe_{0.96}Ru_{0.04})$ 2: formation of a magnetic glass. *Phys. Rev. B: Condens. Matter Mater. Phys.* **2005**, *72*, 180401.
(62) Krebs, B.; Mandt, J. Zur Kenntnis des Argyrodit-Strukturtyps: Die Kristallstruktur von Ag_8SiS_6/The Argyrodite Structure Type: The Crystal Structure of Ag_8SiS_6. *Z. Naturforsch., B: J. Chem. Sci.* **1977**, *32*, 373−379.
(63) Eulenberger, G. Die Kristallstruktur der Tieftemperaturmodifikation von Ag_8GeS_6. *Monatsh. Chem.* **1977**, *108*, 901−913.
(64) Dronskowski, R.; Bloechl, P. E. Crystal orbital Hamilton populations (COHP): energy-resolved visualization of chemical bonding in solids based on density-functional calculations. *J. Phys. Chem.* **1993**, *97*, 8617−8624.

https://doi.org/10.1021/acs.inorgchem.1c03158
Inorg. Chem. 2021, 60, 19345−19355